Dan *et al. Microstructures* **2025**, *5*, 2025050
DOI: 10.20517/microstructures.2024.131

Microstructures

Research Article

Open Access

Check for updates

Enhancing energy storage performance in tungsten bronze ceramics utilizing site engineering

Yuejun Dan[1,2], Liupan Tang[1,2], Wenzhi Ning[1,2], Changzheng Hu[1,2,3], Laijun Liu[1,2,3], Liang Fang[1,2,3]

[1]Key Laboratory of Nonferrous Metal Oxide Electronic Functional Materials and Devices, Education Department of Guangxi Zhuang Autonomous Region, College of Materials Science and Engineering, Guilin University of Technology, Guilin 541004, Guangxi, China.
[2]Guangxi Key Laboratory of Optical and Electronic Materials and Devices, Guilin University of Technology, Guilin 541004, Guangxi, China.
[3]Collaborative Innovation Center for Exploration of Nonferrous Metal Deposits and Efficient Utilization of Resources in Guangxi, Guilin University of Technology, Guilin 541004, Guangxi, China.

Correspondence to: Prof. Changzheng Hu, Key Laboratory of Nonferrous Metal Oxide Electronic Functional Materials and Devices, Education Department of Guangxi Zhuang Autonomous Region, College of Materials Science and Engineering, Guilin University of Technology, Jiangan Road 12, Guilin 541004, Guangxi, China. E-mail: huchzh@foxmail.com

How to cite this article: Dan, Y.; Tang, L.; Ning, W.; Hu, C.; Liu, L.; Fang, L. Enhancing energy storage performance in tungsten bronze ceramics utilizing site engineering. *Microstructures* **2025**, *5*, 2025050. https://dx.doi.org/10.20517/microstructures.2024.131

Received: 20 Nov 2024 **First Decision:** 12 Dec 2024 **Revised:** 20 Dec 2024 **Accepted:** 27 Dec 2024 **Published:** 18 Apr 2025

Academic Editor: Dawei Wang **Copy Editor:** Fangling Lan **Production Editor:** Fangling Lan

Abstract

Advanced electronic systems and innovative pulsed power applications are driving the rapid development of high-energy-storage density and high-efficiency capacitors. In the present study, we have prepared $SrBa_{3.5}Sm_{0.5}R_{0.5}Nb_{9.5}O_{30}$ (R = Mn, Ti, Sn, Hf) (henceforth referred to as SBSRN) ceramics by solid-phase synthesis, using a site engineering strategy that utilizes tetravalent ions for the substitution of Nb^{5+} at the B-site of tetragonal phase tungsten bronzes. SBSRN ceramics benefit from site engineering strategies to enhance overall energy storage performance. As a result, they achieve a substantial energy storage density of 4.31 $J{\cdot}cm^{-3}$ and an impressive efficiency of 91.3% when subjected to an electric field of 340 $kV{\cdot}cm^{-1}$, and show excellent stability in ferroelectric performances with variable temperature and frequency. In addition, these ceramics have a large discharge energy density of 2.68 $J{\cdot}cm^{-3}$ and a fast discharge time of 62 ns in charge/discharge tests, along with a current density of 619.96 Acm^{-2} and a power density of 65.1 $MWcm^{-3}$. In summary, this research offers a promising method for developing energy storage materials that hold potential for innovative applications in pulsed power components.

Keywords: Energy storage, relaxor ferroelectric, ion substitution, tungsten bronze structure

INTRODUCTION

As a functional electronic material that can store and convert transform under an applied electric field, dielectric ceramics serve a crucial role in fields such as aerospace, pulsed power systems, electromagnetic catapults, hybrid vehicles, and electronic communications[1,2]. The growing demand for high-quality dielectric capacitors has given a great impetus to the study of dielectric ceramics with properties such as high efficiency, high energy storage density, large power density (P_D), and rapid discharging times[3-5]. Dielectric ceramics as energy storage materials are not only able to withstand higher voltages, but also have high P_D and fast charging and discharging characteristics. Importantly, dielectric ceramic capacitors offer the advantage of a longer service life than supercapacitors and batteries[6,7]. Compared to a range of dielectric materials such as ferroelectrics, anti-ferroelectrics and linear dielectrics, relaxation ferroelectric ceramics stand out for their excellent temperature stability, high-energy-storage density accompanying high efficiency[8-10]. Among these materials, tungsten-bronze (TB) ferroelectric ceramics have attracted significant attention owing to the flexibility in adjusting the structure and properties through multiple crystallographic positions[11-13]. These ceramics have the structure $(A1)_2(A2)_4(C)4B_{10}O_{30}$, connected by the common vertices of the oxygen octahedra resulting in three different crystal positions: pentagonal (A2), tetragonal (A1), and triangular (C), which gives TB ceramics a complex structure and a rich compositional modulation and leads to a wealth of electrical properties[14,15]. It has been shown that the improvement in the electrical properties of TB can be achieved by the ordered/disordered arrangement of cations with varying oxidation states and size, which arises from the coexistence of its A-site and B-site cations[16-18]. The smaller the difference in ionic radius between the A-sites of TB ceramics, the easier it is to induce relaxor ferroelectric behavior[18-20]. In addition, the main source of ferroelectricity is mainly due to the movement and deflection of the BO_6 octahedron along the c-axis caused by the ions occupying the B-site[21,22]. Therefore, the ferroelectric properties of TB ceramics can be optimized by doping different elements in the A-site and B-site or by changing the radius of the dopant ions.

Ion doping substitution at the A-site and B-site crystallographic positions of TB ceramics to achieve high maximum polarization (P_{max}) and low remanent polarization (P_r) is a key factor in obtaining excellent energy storage properties. Cao *et al.* investigated TB ceramics doped with $Ca_{0.28}Ba_{0.72}Nb_2O_6$ with different radius ions, tuning the relaxor behavior to significantly improve the energy storage performance. The final energy storage performance was obtained with a storage density of W_{rec} ~ 2.59 J·cm^{-3}, an efficiency of η ~ 85.3 %, and a P_D of ~ 130.78 MWcm^{-3}[23]. Peng *et al.* proposed a multi-scale regulation approach in unfilled tetragonal tungsten bronze (TTB) $Sr_{0.425}La_{0.1\gamma0.05}Ba_{0.425}Nb_{1.4}Ta_{0.6}O_6$ ceramics to enhance the energy storage capabilities at the grain, domain, and macroscopic scales. This method resulted in outstanding energy storage performance, achieving an energy storage density of 5.895 J·cm^{-3} and an efficiency of 85.37%[24]. Hou *et al.* discovered that Sb^{5+} substituted unfilled TB $Ca_{0.5}(Sr_{0.5}Ba_{0.5})_2Nb_{5-x}Sb_xO_{15}$ ceramics; the crystal structure transitions from tetragonal *P4bm* to rhombohedral *Ama2* and then to tetragonal *P4/mbm* symmetry. The primary factors contributing to the relaxor behavior in these materials are the *Ama2* phase and the emergence of polar nanoregions (PNRs). These characteristics result in exceptional energy storage performance, with a density of 2.38 J·cm^{-3} and an efficiency of 85%[25]. Xu *et al.* prepared a series of $Sr_2Na_{0.85}Bi_{0.05}Nb_{5-x}Ta_xO_{15}$ (SBNN-xTa) ferroelectric ceramics, which were used to induce structural deformations, ordered/disordered distributions, and polarization modulation through a site engineering strategy of B-site Ta-displaced Nb for enhancing the relaxor behavior. These resulted in an energy storage density of approximately 1.6 J·cm^{-3} and an efficiency of around 80%[26]. Dan *et al.* enhanced the structural distortion and ordered/disordered arrangement in the system through co-substitution with Ba^{2+}, Sm^{3+} and Mn^{4+}, ultimately achieving a high energy storage density of 4.432 J·cm^{-3} in $Sr_2NaNb_5O_{15}$-based ceramics[16].

In this study, SBSRN ceramics were prepared using a site engineering approach. This method involved co-doping the A-site with Ba^{2+}, $Sr^{2+}$and Sm^{3+} ions to synthesize unfilled TB structures. Additionally, the B-site underwent substitution of Nb^{5+} with various tetravalent ions, including Mn^{4+}, Ti^{4+}, Sn^{4+}, and Hf^{4+}. The relaxor ferroelectric behavior of $SrBa_{3.5}Sm_{0.5}R_{0.5}Nb_{9.5}O_{30}$ (R = Mn, Ti, Sn, Hf) (SBSRN) ceramics was induced by increasing the degree of system disorder and enhancing the degree of distortion of BO_6 oxygen octahedra to obtain excellent energy storage performance[27,28]. A combination of XRD, Rietveld structure refinement, transmission electron microscopy (TEM), and Raman reveals that the SBSRN ceramics obtain high efficiency as the radius of the B-site dopant ions induces an increase in the crystallite spacing and the degree of octahedral distortion. Among them, the SBSTN ceramics have high energy storage density of approximately 4.31 J·cm^{-3} and high efficiency of about 91.3 % because SBSTN have high dielectric constants, and show excellent stability in ferroelectric temperature variation and frequency variation tests. In the charge/discharge test, the SBSTN ceramics demonstrate excellent performance, including a discharge energy density (W_{dis}) reaching 2.68 J·cm^{-3}, a current density (C_D) of up to 619.96 Acm^{-2}, a P_D of 65.1 MWcm^{-3} and a rapid discharge time ($t_{0.9}$) of 62 ns.

MATERIALS AND METHODS

The SBSRN compounds were synthesized using high-purity raw materials including $SrCO_3$ (99.95%), $BaCO_3$ (99.95%), Sm_2O_3 (99.99%), MnO_2 (99.95%), TiO_2 (99.99%), SnO_2 (99.99%), HfO_2 (99.99%), and Nb_2O_5 (99.99%) in stoichiometric ratios as determined by their respective compositions. Anhydrous ethanol and ZrO_2 were used as the ball milling media in a high-energy ball milling tank. The raw materials, weighed according to their stoichiometric ratios, were mixed and subjected to high-energy ball milling for 6 h. The resulting ball-milled slurry was subsequently dried in an oven at 120 °C. The dried slurry was pressed into a 20 mm diameter column using a mold and calcined at 1,000 °C for 4 h to ensure that the main crystalline phase could be initially synthesized. In order to further improve homogeneity and reduce particle size, secondary ball milling using a high-energy ball mill was again used, and the drying of the secondary ball milled slurry was again placed in an oven at 120 °C. The slurry was then dried. Finally, the dried powder was subjected to cold isostatic pressing (256 MPa, 10 min) to form particles with a diameter of about 8 mm, and then sintered at temperatures ranging from 1,250~1,370 °C to obtain dense ceramic samples. Among them, in the electrical performance test, the thickness of the dielectric constant test sample was 1.2 mm (± 0.1 mm); the electrode area was 50.24 mm^2, and the thickness of the ferroelectricity and charge/discharge test sample was 0.08 mm (± 0.01 mm); the electrode area was 3.14 mm^2.

The physical phase of SBSRN ceramics was determined by X-ray diffractometry (PANalytical, Empyrean Cu Kα1). The microscopic surface morphology and energy dispersive X-ray spectroscopy (EDS) of the samples were acquired using an emission scanning electron microscope (Hitachi S-4800). Raman spectra were recorded using a DXR laser confocal Raman spectrometer (Thermo Fisher Scientific). The 8 mm diameter ceramic samples were polished and coated on both sides with silver paste electrodes and sintered at 650 °C for 30 min. X-ray photoelectron spectroscopy (XPS) data was obtained using Thermo Fisher ESCALAB 250Xi equipment on the powdered ceramic samples. Ferroelectric polarization hysteresis loops were acquired with a ferroelectric workstation at room temperature and a frequency of 10 Hz (TF 2000E Analyzer, Aix ACCT). The temperature characteristics of dielectric constant (ε_r) and dielectric loss (tanδ) were measured using a precision LCR meter (TZDM-200-300, Harbin Julang Technology). The charge/discharge performance was assessed using a dielectric charge test system (CFD-005, TG Technologies). TEM analysis was employed to examine the surface morphology of the powders by a transmission electron microscope (JEM 2100F, JEOL).

RESULTS AND DISCUSSION

Figure 1A shows the phase structure of SBSRN ceramics. The XRD diffraction peaks of the SBSRN ceramic samples are in excellent agreement with those of the standard cards (COD#96-400-1509); all the samples have a single tetragonal TB structure with a *P4bm* space group. Figure 1B shows a local zoom in from 31° to 33° where a shift of the XRD peaks towards lower angles can be clearly observed, indicating an increase in the crystal spacing d, which is attributed to the increase in the coordination radius of the B-site atoms.

The Rietveld refinement results of the XRD data of SBSRN ceramic powders are shown in Figure 2A-D and Table 1, where R_p < 10% and R_{wp} < 10%, indicating that the results are reliable[29,30]. Moreover, as the ionic radius of the dopant ions on the B-site increases leading to an increase in the cell volume, this is in agreement with the above analysis of the XRD results.

Due to the large difference in the radius of the B-site ions shown in Table 1, we further take the EDS energy spectrum analysis to support the rationality of the doping. A uniform distribution of all elements can be seen in Figure 3. In addition, the microscopic morphology of the grains demonstrated by the SEM patterns can be observed to be relatively homogeneous and dense and without obvious pore formation for each ceramic sample. The average grain sizes of the SBSRN ceramic samples were 2.50, 2.08, 2.09, and 2.36 μm, respectively.

The feasibility of doping elements with large differences in ionic radii at the B-site was analyzed by XRD and EDS energy spectroscopy, and then we performed Raman scattering spectroscopy tests on the SBSRN ceramic samples to analyze the structure and phase of the SBSRN ceramic as shown in Figure 4. The characteristic peak shape associated with the tetragonal phase of TB is evident. Here, v1 and v2 correspond to the R/Nb-O stretching modes, while v5 represents the O-R/Nb-O bending mode. Vibrations resulting from the movement of the A-site cations relative to the BO_6 octahedron occur at wave numbers below 200 cm^{-1}[31-33]. As shown in the direction of the arrow in Figure 4A, the expansion of the R/Nb-O_6 octahedral lattice, driven by the increased ionic radius of the B-site, which consequently leads to a weakening of the interactions between the R/Nb and O atoms within the R/Nb-O_6 octahedron. Consequently, the vibrational modes of v5 and v2 exhibit a slight shift to the right. This effect makes the BO_6 octahedra more susceptible to deformation and twisting along the c-axis, thereby inducing the relaxor ferroelectric behavior of SBSRN in ceramics[34]. This behavior ensures a low P_r, leading to enhanced energy storage efficiency. The full width at high maximum (FWHM) in SBSRN ceramics was calculated by fitting each Raman spectrum using Gaussian functions, as illustrated in Figure 4B and C. It is evident that the FWHM grows with the increase in the B-site ionic radius, suggesting a higher degree of distortion in the BO_6 octahedra.

The high-resolution TEM (HRTEM) images and electron diffraction of selected regions of the SBSRN ceramic are shown in Figure 5, in which the diffraction spots were able to complete the calibration of the spatial group at *P4bm*, which further verified that the synthesized ceramic samples were TTB structure.

As illustrated in Figure 5A, D, E, H, SBSMN and SBSHN ceramics were analyzed using HRTEM and electron diffraction techniques in selected regions along the [110] zone axis. The lattice spacings at the (110) crystal plane were determined to be 0.947 and 0.950 nm, respectively. For SBSTN and SBSSN ceramics, HRTEM and electron diffraction analyses were conducted on selected regions along the [220] zone axis, as depicted in Figure 5B, C, F, G. These analyses confirmed the corresponding lattice spacings of the (220) crystal plane to be 0.429 and 0.430 nm, respectively. TEM testing revealed that the substitution of large-radius ions at the B-site can lead to an increase in the crystal plane spacing, which aligns well the finding from XRD analysis Rietveld refinement.

Table 1. Ion radius and Rietveld refinement results for SBSRN ceramics

	R = Mn	R = Ti	R = Sn	R = Hf
Radii (Å)	0.53	0.605	0.69	0.71
R_p (%)	4.46	4.02	4.30	4.11
R_{wp} (%)	6.60	5.76	6.18	5.91
a (Å)	12.4861(1)	12.4945(6)	12.4949(4)	12.5014(0)
b (Å)	12.4861(1)	12.4945(6)	12.4949(4)	12.5014(0)
c (Å)	3.9483(0)	3.9467(9)	3.9468(2)	3.9493(3)
V (Å^3)	613.778(1)	616.149(3)	616.191(5)	617.221(0)

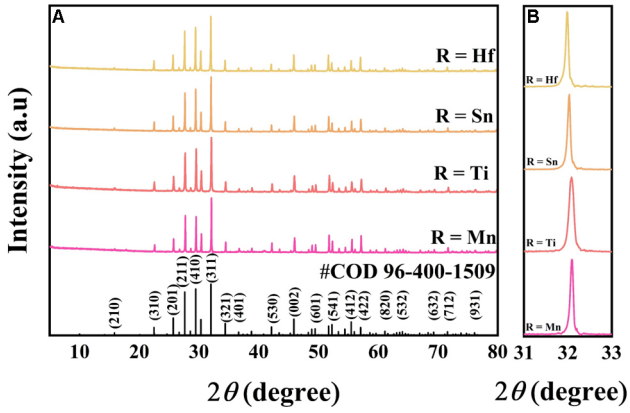

Figure 1. (A) XRD patterns of SBSRN ceramics and (B) the enlarged patterns at the 2theta angle of 31°-33°.

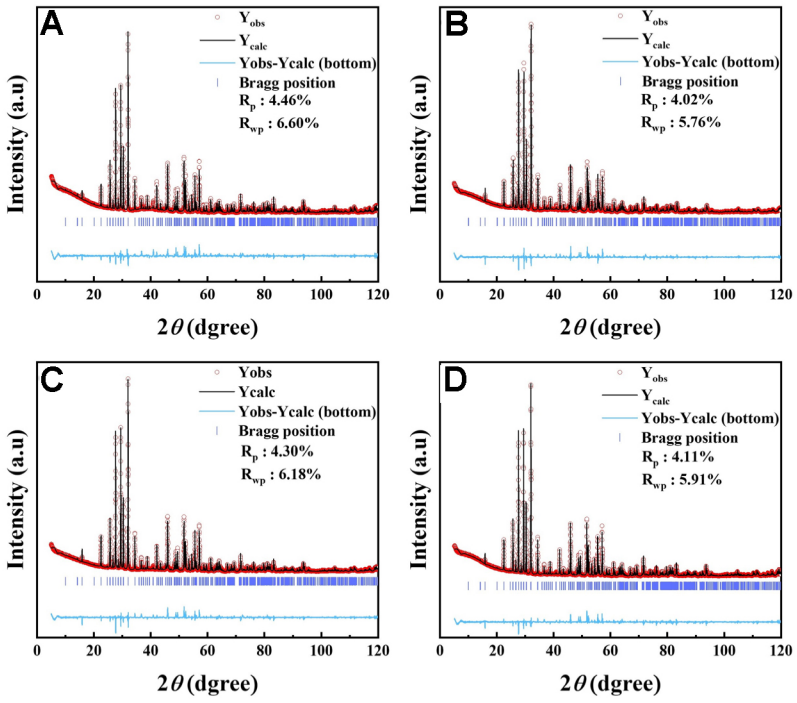

Figure 2. (A-D) Rietveld refinement plots of SBSRN ceramics, where Y_{obs} is the experimental measurements value, Y_{calc} is the calculated measurement value, Y_{obs}-Y_{calc} are the difference values, R_p is the profile factor, and R_{wp} is the weighted-profile factor.

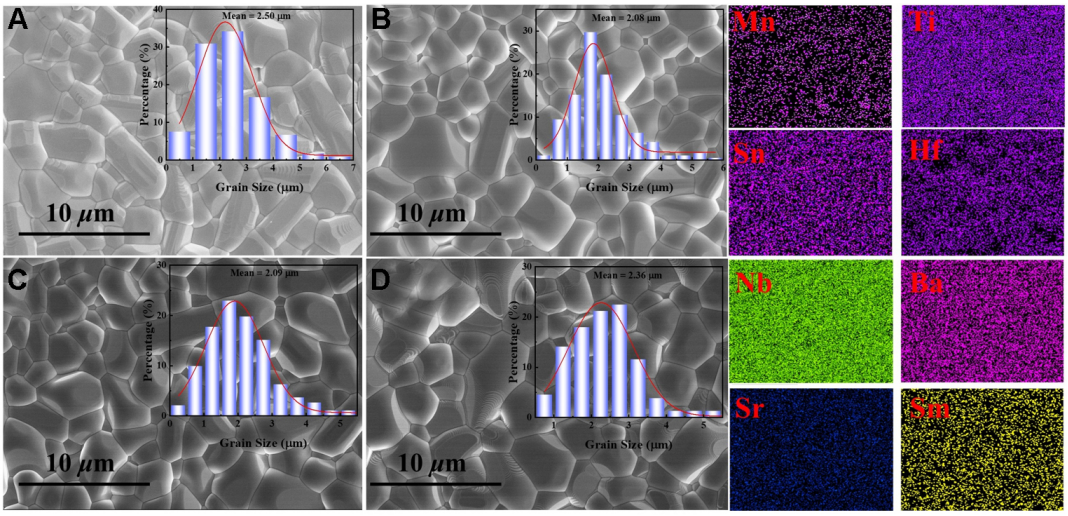

Figure 3. SEM and EDS spectra of SBSRN ceramics, (A) R = Mn, (B) R = Ti, (C) R = Sn, (D) R = Hf.

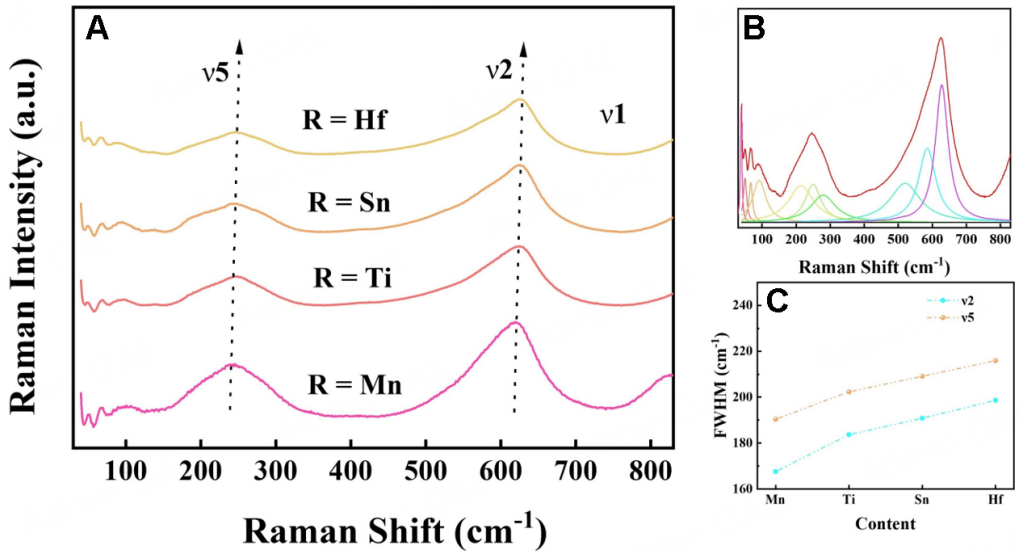

Figure 4. (A) Raman spectra of SBSRN ceramics at room temperature, (B) Results of Gaussian fitting of Raman peaks, (C) FWHMs of ν2 and ν5 modes of different component samples.

The variation of dielectric properties of SBSRN ceramics with temperature was measured at -160~250 °C, as shown in Figure 6A-D. The increase in temperature results in a frequency dispersion of the dielectric constant, which exhibits typical dielectric relaxor properties[35]. In addition to the low-temperature diffuse phase transition, SBSMN ceramics also have a ferroelectric phase to paraelectric phase transition at high temperatures[36], due to the combined effect of both of which results in SBSMN ceramics having excellent temperature stability at -43~165 °C, as shown in Figure 6A. In addition, SBSHN ceramics comply with the X7R capacitor standard from -80 to 130 °C due to having a low dielectric constant, as shown in Figure 6E.

In the comparison of SBSRN ceramics, SBSTN ceramics have the highest dielectric constant, with a peak dielectric constant of over 2,400 (ε_m). A high dielectric constant is usually accompanied by a high polarization, a property that is advantageous for the improvement of energy storage density. On the other

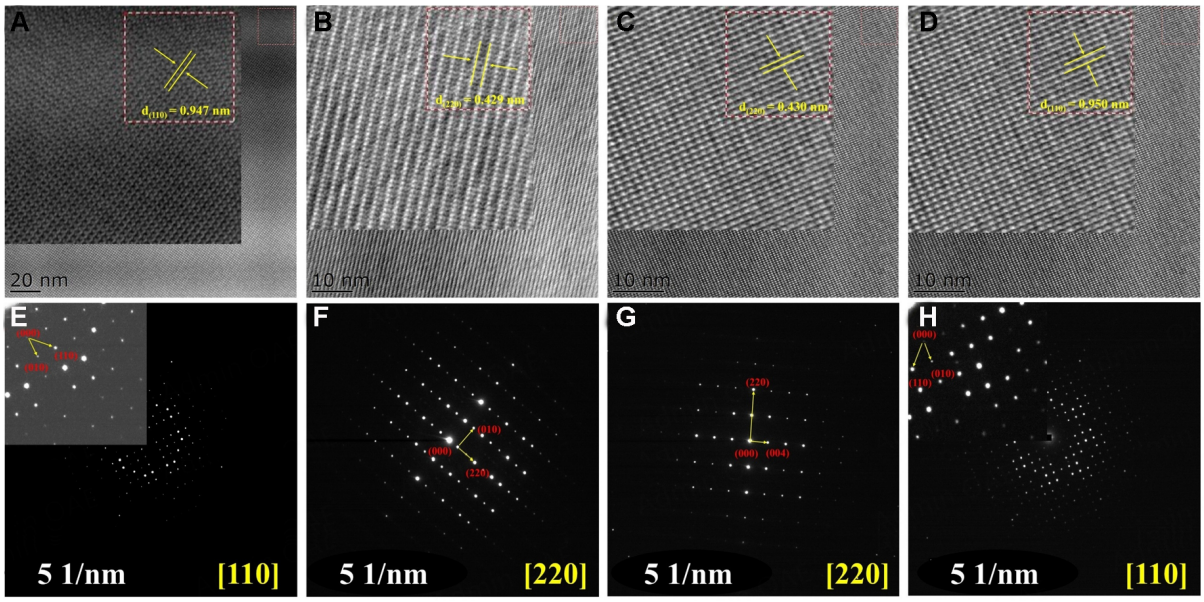

Figure 5. (A-D) HRTEM image and (E-H) Electron diffraction patterns of selected regions of SBSRN (R = Mn,Ti,Sn,Hf) ceramics.

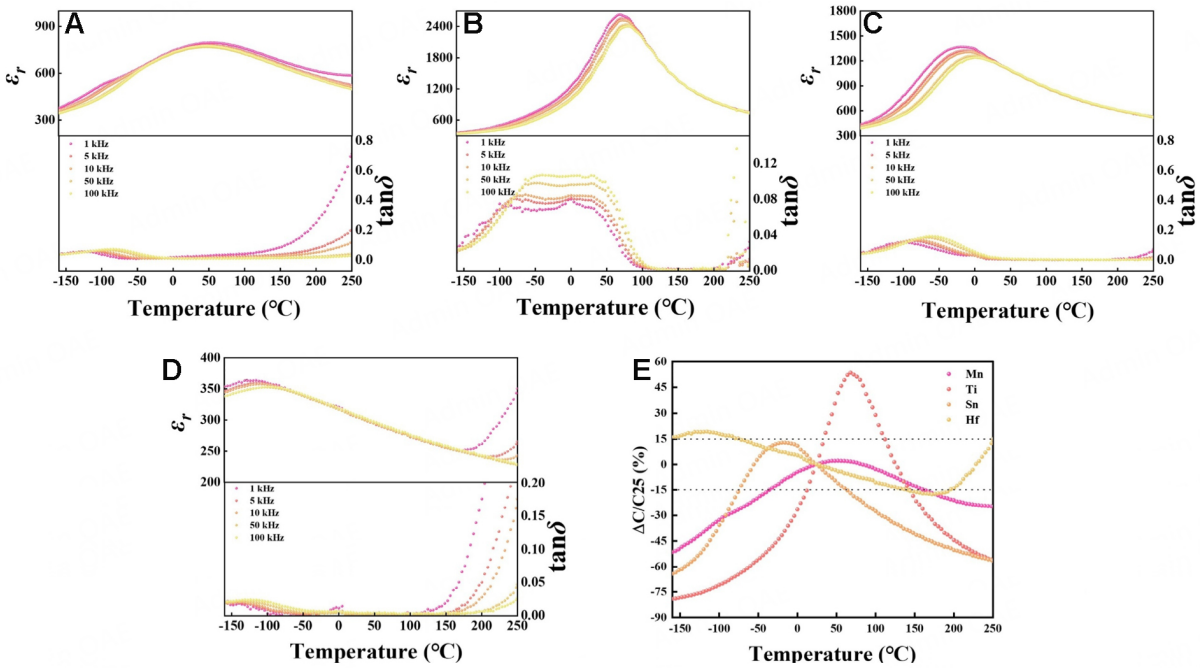

Figure 6. The temperature-dependent behavior of dielectric properties, (A) R = Mn, (B) R = Ti, (C) R = Sn, (D) R = Hf, (E) variation rate of dielectric constant of SBSRN ceramics at 1 kHz.

hand, SBSSN and SBSHN ceramics have lower Curie peak temperatures and exhibit a paraelectric phase above room temperature, which may be detrimental to energy storage density.

As shown in Figure 7A-D, a macroscopic phenomenological statistical model was used to match the dielectric constant of SBSRN ceramics at 1 kHz. This approach aimed to elucidate how doping at the B-site with different ionic coordination radii influences the dielectric behavior of tetragonal-phase TB ceramics,

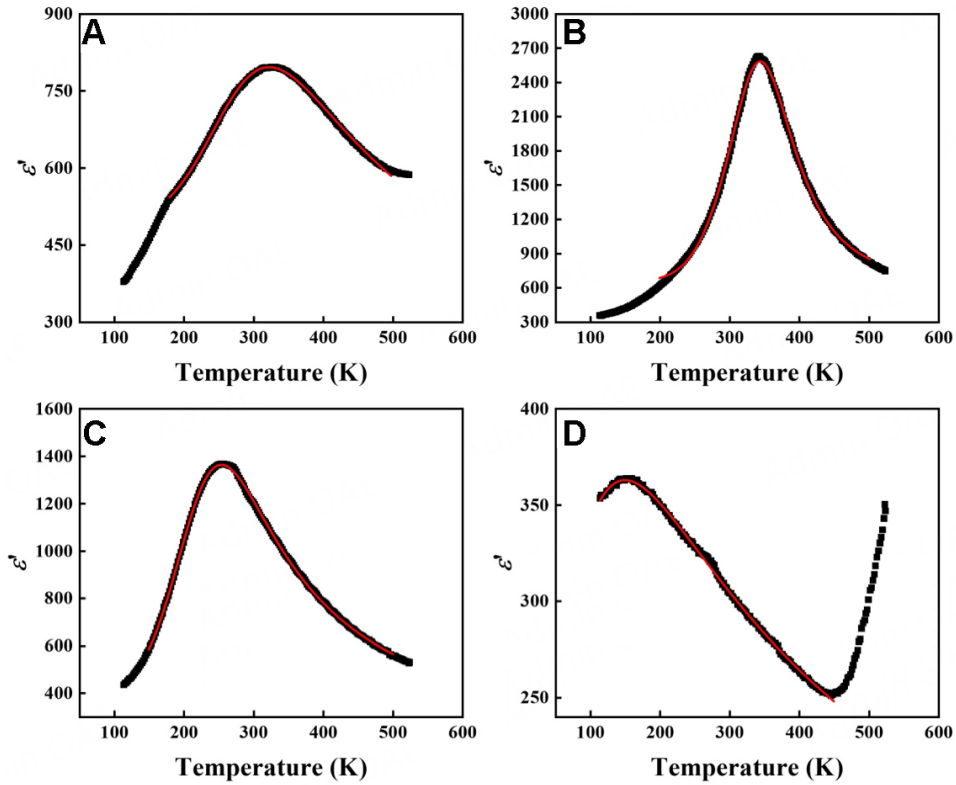

Figure 7. Macroscopic phenomenological statistical models fitting of the dielectric constant of SBSRN ceramics at 1 kHz, (A) R = Mn, (B) R = Ti, (C) R = Sn, and (D) R = Hf.

specifically in terms of dipole thermodynamic behavior. The fitting results, represented by the red line, exhibit a strong correlation with the temperature-dependent dielectric constant curve, denoted by the black line. This model employs an average potential well depth (E_b) to elucidate the mechanism by which PNR dipole contributes to polarization. The E_b value is strongly associated with the volume of the PNR, and the dipole energy follows the Maxwell-Boltzmann distribution. The relationship between the number of activated state dipoles, N_1 (E_b, T), and the number of dipoles confined within the potential well, N_2 (E_b, T), is determined by[33,37]

$$N_1(E_b,T) = N\sqrt{\frac{4}{\pi}}\sqrt{\frac{E_b}{K_bT}}exp(-\frac{E_b}{K_bT}) + Nerf\sqrt{\frac{E_b}{K_bT}} \quad (1)$$

$$N_2(E_b,T) = N - N_1(E_b,T) \quad (2)$$

where N stands for the total number of dipoles in the system, k_B is the Boltzmann constant, and T indicates absolute temperature. ε_1, ε_2, b, and θ are constants, and P_1 and P_2 are the variations in the dipole with the temperature at a frequency of 1 kHz. while the dipoles are also considered. The relationship between dielectric constant and temperature is given in

$$\varepsilon(T) = \frac{\varepsilon_1}{1+bexp\left(-\frac{\theta}{T}\right)}P_1(E_b,T) + \varepsilon_2 P_2(E_b,T) \quad (3)$$

The volume of the PNR is determined using the depth of the potential well (E_b), which is derived from the fitting of the model and the Landau-Devonshire free energy equation:

$$E_b = \Delta G_v \times V \tag{4}$$

Here, ΔG_v ranges from 10^5 to 10^7 J m^{-3}, and V represents the volume of each PNR. The results of the calculations are shown in Table 2.

As shown in Table 2, the PNR volume is progressively declining; however, an anomaly occurs in SBSTN ceramics, when its PNRs are significantly higher than the other three compounds.

By comparing the dielectric constant versus temperature in Figure 6A-D, we found that the dielectric constant peak of SBSTN is relatively sharp, so we fitted the dielectric constant at 1 kHz according to the modified Curie-Weiss law and evaluated the relaxor properties of SBSRN ceramics through the dispersion coefficient, as defined by the law in[38,39].

$$ln(1/\varepsilon - 1/\varepsilon_m) = \gamma ln(T - T_m) \tag{5}$$

where T_m, ε_m and γ represent the peak dielectric temperature, the maximum dielectric constant, and the dispersion coefficient, respectively. The value of γ typically falls between 1 and 2 for the relaxor ferroelectric. As illustrated in Figure 8A-D, the fitted values of γ are all greater than 1 and less than 2, indicating dielectric relaxor behavior.

Based on the fitting results, it was found that SBSTN ceramics have the lowest γ, and the reason for this may be due to the larger volume of PNRs of SBSTN ceramics compared to that of other SBSRN ceramics, which results in a relatively sharp dielectric peak.

Figure 9A illustrates the P-E hysteresis loops of the SBSRN ceramic measured at the electric strength corresponding to the breakdown field, whereas Figure 9B presents the specific energy storage density and energy storage efficiency. It was observed that the doping with tetravalent cations at the B-site causes a distortion in the BO_6 octahedral structure, leading to local structural order/disorder. This disruption affects the long-range ferroelectric ordering, resulting in the formation of PNRs and imparting relaxor ferroelectric properties to the SBSRN ceramics. These PNRs help maintain low P_r values in the ferroelectric ceramics. The energy storage characteristics of SBSRN ceramics were determined using[40-42].

$$W_{total} = \int_0^{P_{max}} EdP \tag{6}$$

$$W_{rec} = \int_{P_r}^{P_{max}} EdP \tag{7}$$

$$\eta = \frac{W_{rec}}{W_{total}} \times 100\% \tag{8}$$

Based on these calculations, the SBSMN ceramic has an energy storage density of 1.34 J·cm^{-3} and an efficiency of 82.3% when subjected to a breakdown electric field of 200 kV·cm^{-1}. In comparison, the breakdown electric fields for SBSTN, SBSSN, and SBSHN ceramics are approximately 350 kV·cm^{-1}, with corresponding energy storage densities of 4.31, 3.19, and 2.84 J·cm^{-3}, respectively. These materials also demonstrate high efficiencies, specifically 91.3%, 91.3%, and 95.2%, respectively. The elevated high energy storage density in SBSTN ceramics can be attributed to their high dielectric constant (ε_m > 2400), whereas the superior efficiency in SBSTN, SBSSN and SBSHN ceramics is due to the reduced volume of the PNRs.

Table 2. The dielectric constant parameters of SBSRN ceramics

	R = Mn	R = Ti	R = Sn	R = Hf
E_b (eV)	0.095	0.204	0.079	0.039
V ($\times 10^{-27}$ m^3)	1.52	3.27	1.27	0.63

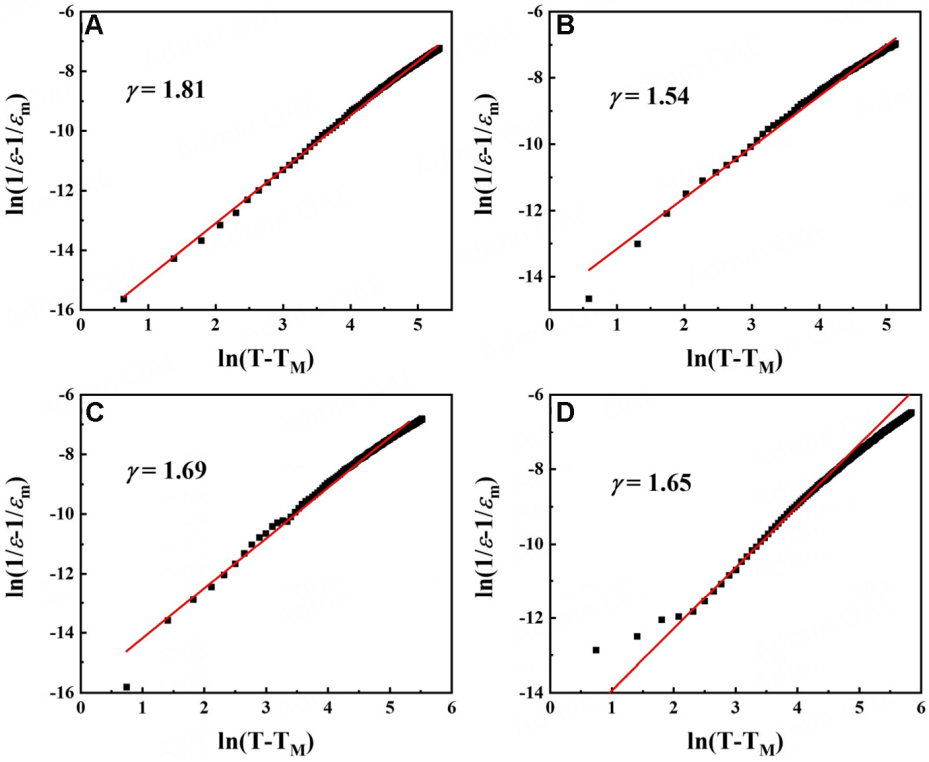

Figure 8. The 1 kHz dielectric constant fitting using a modified Curie-Weiss law, (A) R = Mn, (B) R = Ti, (C) R = Sn, and (D) R = Hf.

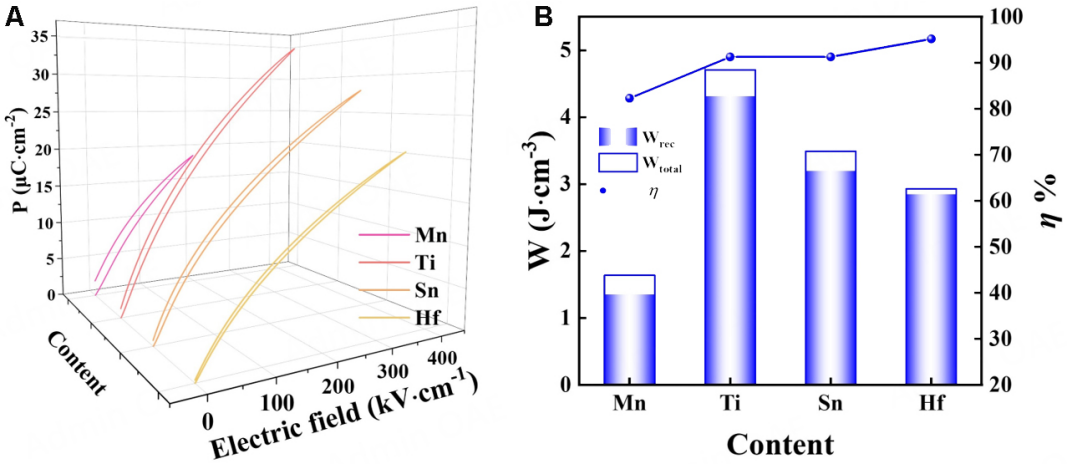

Figure 9. (A) Hysteresis loops of SBSRN ceramics, (B) The specific energy storage density and energy storage efficiency of SBSRN ceramics.

In order to explore the intrinsic factors that make the breakdown electric field of SBSMN ceramics lower than that of the other three groups of SBSRN ceramics, we tested the X-ray electron spectra of SBSMN ceramics.

Figure 10A shows the X-ray electron spectra of Mn $2p_{3/2}$ and Mn $2p_{1/2}$ of SBSMN ceramics near 642.0 and 653.3 eV, indicating the presence of Mn ions. The successful fitting of the two characteristic peaks of Mn^{2+} and Mn^{3+} in the Mn-2p orbitals indicates the presence of a valence change behavior of Mn^{4+} which induces a ferroelectric decay effect, which may be responsible for the dielectric anomalies at low temperatures of the SBSMN ceramics, which therefore have excellent dielectric temperature stability. The valorization of Mn^{4+} causes an increase in oxygen vacancies with the reactions:

$$Mn^{4+} + e' = Mn^{3+} \quad (9)$$

$$Mn^{4+} + 2e' = Mn^{2+} \quad (10)$$

$$O_O = V_O^{\cdot\cdot} + 2e' + 1/2O_2 \quad (11)$$

Figure 10B illustrates four distinct peaks at binding energies of approximately 529.5, 532, 532.5 and 533.5 eV, corresponding to lattice oxygen, oxygen vacancies absorbed by-OH, C-O bonds, and absorbed oxygen (surface H_2O), respectively[43,44]. This indicates that Mn^{4+} ions contribute to the formation of oxygen vacancies, and these oxygen vacancy defects result in leakage conduction in dielectric ceramic materials, thereby reducing the breakdown electric field of SBSMN ceramics.

Variable-temperature ferroelectric measurements were performed on SBSRN ceramics, as shown in Figure 11A-D, using electric fields of 90, 150, 150, and 200 kV·cm^{-1}, respectively. All these tests were conducted at a frequency of 10 Hz. The presence of valence-changing behavior results in an increase in dipole defects, leading to the loss of ferroelectric properties at elevated temperatures and a significant reduction in the energy storage density and efficiency of SBSMN ceramics during variable-temperature ferroelectric tests (see Figure 11A and E). As illustrated in Figure 11B, for SBSTN ceramics, the polarization value exhibits a fluctuating trend across different temperatures, peaking at 17.5 μC/cm^2 at 50 °C during the variable temperature ferroelectric characterization. Furthermore, as shown in Figure 11F, the energy storage density of the SBSTN ceramics reaches its highest point of 1.02 J·cm^{-3} at 90 °C, with an efficiency of 95.6%. Additionally, the ferroelectric properties of SBSTN ceramics demonstrate excellent temperature stability, varying by no more than 5% throughout the tested temperature range. From Figure 11C, it is observed that as the temperature increases, the hysteresis loop of SBSSN ceramics initially rises and then subsequently declines at the point of P_{max}. Meanwhile, the P_r shows a steady increase, resulting in a significant decrease in both its energy storage density and efficiency. In conjunction with the relationship between the variation of dielectric constant and temperature, it is evident that SBSSN ceramics remain in the ferroelectrics phase throughout the variable-temperature ferroelectric testing range at a frequency of 10 Hz. In addition, the sharp decrease in dielectric constant leads to a significant decrease in its energy storage density and efficiency, so that the storage density of SBSSN ceramics decreases from 0.95 J·cm^{-3} at 30 °C to 0.74 J·cm^{-3} at 120 °C, corresponding to a decrease in efficiency from 95.2% to 62.5%, as shown in Figure 11G. Similar to SBSSN ceramics, SBSHN ceramics were also in the paraelectric phase during the temperature interval tested, with the P_{max} decreasing with increasing temperature, but the SBSHN ceramics obtained the same excellent ferroelectric temperature stability as the SBSTN ceramics due to the lower rate of change of the dielectric constant with increasing temperature. The energy storage density of SBSHN ceramics reduces from 1.62 to 1.55 J·cm^{-3} with a rate of change that does not exceed 5% and the efficiency drops from 95.38% to 92.4% (see Figure 11H).

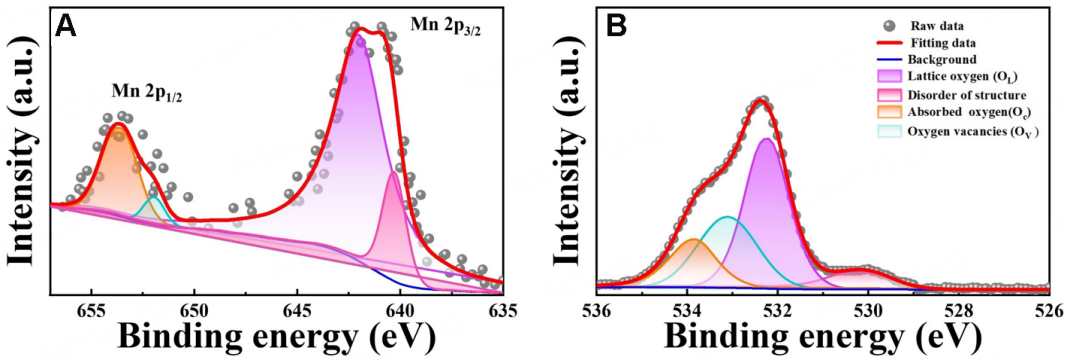

Figure 10. (A) X-ray electron spectroscopy mapping of SBSMN ceramics, (A) Mn, (B) O.

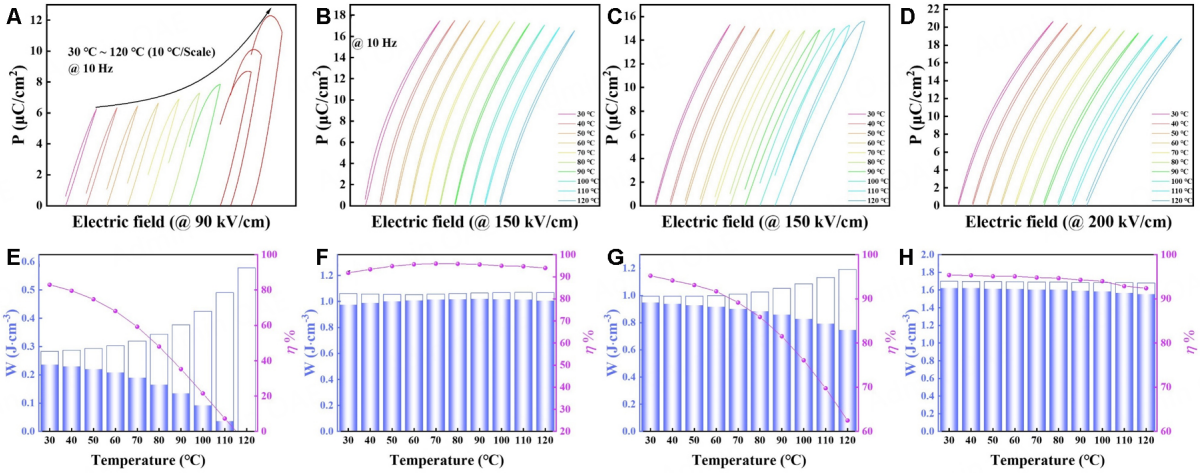

Figure 11. Variable temperature ferroelectric properties of SBSRN ceramics, (A) R = Mn, (B) R = Ti, (C) R = Sn, (D) R = Hf; Energy storage density as well as efficiency of variable temperature ferroelectrics based on SBSRN ceramics, (E) R = Mn, (F) R = Ti, (G) R = Sn, (H) R = Hf.

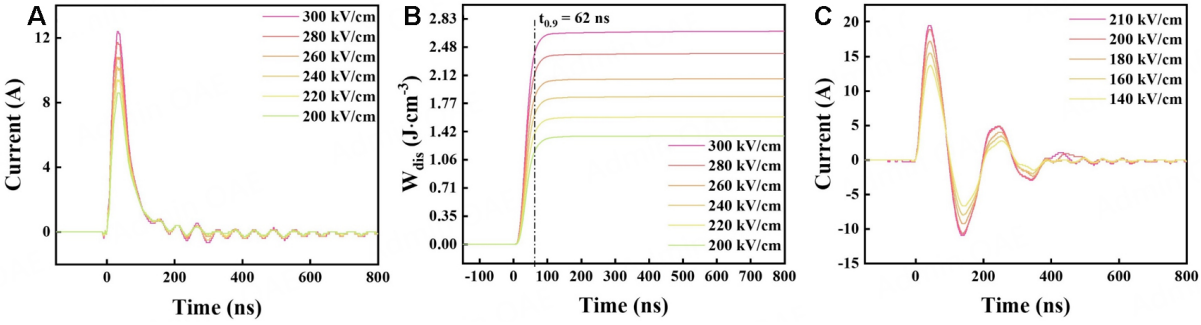

Figure 13. Charge/discharge characteristics of SBSTN ceramics: (A) the overdamping behavior in charge/discharge current curves, (B) the discharge energy density and $t_{0.9}$, (C) the underdamping characteristics of the discharge current.

As shown in Figure 12A, when the frequency is increased from 1 to 200 Hz, the motion of the defective dipole is difficult to follow the frequency change, resulting in a decrease in the P_{max} and P_r of the SBSMN ceramics at high frequencies, but the elongated electric hysteresis return line at high frequencies leads to a significant increase in the energy storage density and efficiency of the SBSMN ceramics (see Figure 12B).

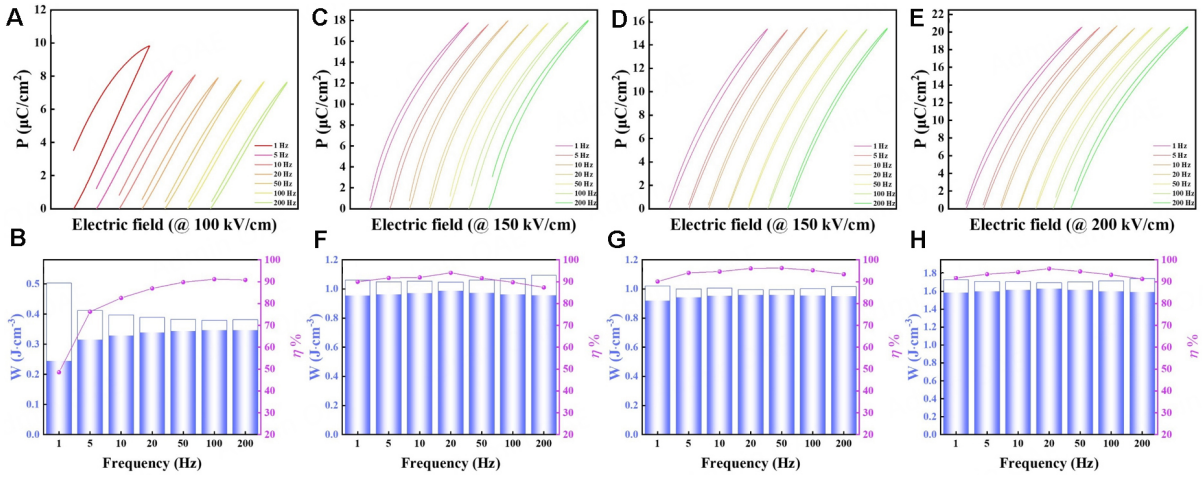

Figure 12. Variable frequency ferroelectric properties of SBSRN ceramics, (A) R = Mn, (C) R = Ti, (D) R = Sn, (E) R = Hf, Energy storage density as well as efficiency of variable temperature ferroelectrics based on SBSRN ceramics, (B) R = Mn, (F) R = Ti, (G) R = Sn, (H) R = Hf.

Fortunately, the change in frequency does not significantly affect the polarization characteristics of the SBSTN ceramics, SBSSN ceramics, and SBSHN ceramics, which is confirmed by the slender P-E curves (see Figure 12C-E). Correspondingly, in Figure 12F-H, the energy storage density and efficiency are maintained at a high level, showing excellent frequency stability. The maximum energy storage density of SBSTN ceramics is 0.98 J·cm^{-3} at 20 Hz, while at 1 Hz, it is 0.95 J·cm^{-3}, and the rate of change can still be maintained below 5%.

After a comprehensive comparison of the electrical properties of SBSRN ceramics, it was found that SBSTN ceramics have superior energy storage properties. To assess their practical application potentials, a range of charge/discharge tests were performed. These tests included measurements of $t_{0.9}$, P_D, W_{dis}, and C_D. The aim is to evaluate how effectively SBSTN ceramics could perform in practical applications.

Therefore, the W_{dis} in the overdamping test can be calculated using [26,45]:

$$W_{dis} = R \int i^2(t)dt/V \tag{12}$$

where R represents the load resistance, with an overdamping value of 140 Ω and an underdamping value of 3 Ω; $i(t)$ denotes the discharge current; V stands for the sample volume.

From Figure 13A, it is evident that the peak current of the overdamped charge and discharge of the SBSTN ceramics rises as the electric field density increases. As observed in Figure 13B, the corresponding W_{dis} also exhibits an upward trend, ultimately achieving a high W_{dis} of 2.68 J·cm^{-3} and a fast charge and $t_{0.9}$ = 62 ns at an electric field strength of 300 kV·cm^{-1}.

It should be highlighted that, for the underdamping test, the C_D and P_D of the SBSTN ceramic capacitors were determined using

$$C_D = I_{max}/S \quad (13)$$

$$P_D = EI_{max}/2S \quad (14)$$

where I_{max} represents the peak current, while S denotes the electrode area[26,45].

The underdamping test of SBSTN ceramics presents a sinusoidal decay waveform for the discharge waveform under each electric field, as illustrated in Figure 13C. Notably, when the electric field reaches 210 kV·cm^{-1}, the peak current is measured at 19.467 A. Consequently, based on Equations (13)-(14), the C_D of SBSTN ceramics is calculated to be 619.96 Acm^{-2}, while the P_D is 65.1 MWcm^{-3}. As a result, SBSTN ceramics have excellent energy storage characteristics and performance in charge/discharge tests, highlighting their promising application as energy storage capacitors.

CONCLUSIONS

In this study, SBSRN ceramics were prepared by site engineering utilizing tetravalent elements to replace Nb^{5+} at the B-site of tetragonal phase TB in conjunction with a solid-phase reaction method. XRD, TEM and Raman tests and Rietveld structure refinement have shown that the crystal plane spacing increases with the coordination radius of TB B-site doped ions, and this strategy is conducive to breaking the ferroelectric long-range ordering. Finally, the SBSTN ceramics, which possess a high dielectric constant, achieved a high energy storage density of 4.31 J·cm^{-3} and an efficiency of 91.3 % under an electric field strength of 340 kV·cm^{-1}, and they also demonstrate excellent stability in ferroelectric variable temperature and frequency tests. The overdamping charge/discharge test reveals that the SBSTN ceramic has a high W_{dis} of 2.68 J·cm^{-3} and a rapid $t_{0.9}$ of 62 ns. In underdamping charge/discharge conditions, the SBSTN ceramics have a C_D of 619.96 Acm^{-2} and a P_D of 65.1 MWcm^{-3}. Consequently, this work highlights the potential of ceramic energy storage capacitors to comprehensively enhance energy storage performance.

DECLARATIONS

Authors' contributions

Design: Hu, C.; Fang, L.
Experiments and data collection: Dan, Y.; Tang, L.; Ning, W.
Data analysis: Dan, Y.; Tang, L.
Manuscript writing: Dan, Y.
Manuscript revision and supervising: Hu, C.; Liu, L.
All authors have read and agreed to the published version of the manuscript.

Availability of data and materials

The data that support the findings of this study are available from the corresponding author upon reasonable request.

Financial support and sponsorship

This work was supported by the National Natural Science Foundation of China (12164012), the Science and Technology Plan of Guangxi (AA25069001), and the Science and Technology Plan of Guilin (ZY20220101).

Conflicts of interest

All authors declared that there are no conflicts of interest.

Ethical approval and consent to participate

Not applicable.

Consent for publication

Not applicable.

REFERENCES

1. Wang, G.; Lu, Z.; Li, Y.; et al. Electroceramics for high-energy density capacitors: current status and future perspectives. *Chem. Rev.* **2021**, *121*, 6124-72. DOI PubMed PMC
2. Sun, Z.; Wang, Z.; Tian, Y.; et al. Progress, outlook, and challenges in lead-free energy-storage ferroelectrics. *Adv. Elect. Mater.* **2020**, *6*, 1900698. DOI
3. Thakur VK, Gupta RK. Recent progress on ferroelectric polymer-based nanocomposites for high energy density capacitors: synthesis, dielectric properties, and future aspects. *Chem. Rev.* **2016**, *116*, 4260-317. DOI PubMed
4. Xiong, X.; Liu, H.; Zhang, J.; et al. Ultrahigh energy-storage in dual-phase relaxor ferroelectric ceramics. *Adv. Mater.* **2024**, *36*, e2410088. DOI
5. Liu, Y.; Liu, J.; Pan, H.; et al. Phase-field simulations of tunable polar topologies in lead-free ferroelectric/paraelectric multilayers with ultrahigh energy-storage performance. *Adv. Mater.* **2022**, *34*, e2108772. DOI
6. Yang, H.; Yan, F.; Lin, Y.; Wang, T. Novel strontium titanate-based lead-free ceramics for high-energy storage applications. *ACS. Sustain. Chem. Eng.* **2017**, *5*, 10215-22. DOI
7. Jayakrishnan, A. R.; Silva, J. P. B.; Kamakshi, K.; et al. Are lead-free relaxor ferroelectric materials the most promising candidates for energy storage capacitors? *Prog. Mater. Sci.* **2023**, *132*, 101046. DOI
8. Peng, H.; Wu, T.; Liu, Z.; et al. High-entropy relaxor ferroelectric ceramics for ultrahigh energy storage. *Nat. Commun.* **2024**, *15*, 5232. DOI PubMed PMC
9. Yang, B.; Liu, Y.; Gong, C.; et al. Design of high-entropy relaxor ferroelectrics for comprehensive energy storage enhancement. *Adv. Funct. Mater.* **2024**, *34*, 2409344. DOI
10. Liu, G.; Li, Y.; Guo, B.; et al. Ultrahigh dielectric breakdown strength and excellent energy storage performance in lead-free barium titanate-based relaxor ferroelectric ceramics via a combined strategy of composition modification, viscous polymer processing, and liquid-phase sintering. *Chem. Eng. J.* **2020**, *398*, 125625. DOI
11. Duan, J.; Wei, K.; Du, Q.; Ma, L.; Qi, H.; Li, H. High-entropy tungsten bronze ceramics for large capacitive energy storage with near-zero losses. *Adv. Funct. Mater.* **2024**, *34*, 2409446. DOI
12. Liu, J.; Jiang, Y.; Zhang, W.; et al. Ferroelectric tungsten bronze-based ceramics with high-energy storage performance via weakly coupled relaxor design and grain boundary optimization. *Nat. Commun.* **2024**, *15*, 8651. DOI PubMed PMC
13. Wan, R.; Zhang, H.; Sheng, L.; et al. Outstanding energy density and charge-discharge performances in $Sr_2KNb_5O_{15}$-based tungsten bronze ceramics for dielectric capacitor applications. *Ceram. Int.* **2024**, *50*, 37126-35. DOI
14. Yang, B.; Gao, Y.; Li, J.; et al. Tailoring Zr-doped tungsten bronze (Sr,Ba,Gd)Nb_2O_6 relaxor ferroelectric with high electrical insulation interface for dielectric capacitor. *Compos. Part. B. Eng.* **2024**, *271*, 111189. DOI
15. Li, S.; Yan, Z.; You, Y.; et al. Enhancement of energy storage and luminescent performances in tungsten bronze multifunctional ceramics. *Ceram. Int.* **2024**, *50*, 14223-31. DOI
16. Dan, Y.; Zheng, X.; Meng, Y.; et al. Simultaneously achieving large energy storage density and high efficiency in the optimized $Sr_2NaNb_5O_{15}$ system with excellent temperature stability at a low electric field. *Ceram. Int.* **2024**, *50*, 6801-13. DOI
17. Dan, Y.; Tang, L.; Ning, W.; et al. Achieving enhanced energy storage performance and ultra-fast discharge time in tungsten-bronze ceramic. *J. Adv. Ceram.* **2024**, *13*, 1349-58. DOI
18. Feng, W. B.; Zhu, X. L.; Liu, X. Q.; Chen, X. M. Effects of B site ions on the relaxor to normal ferroelectric transition crossover in $Ba_4Sm_2Zr_4(Nb_xTa_{1-x})_6O_{30}$ tungsten bronze ceramics. *Appl. Phys. Lett.* **2018**, *112*, 262904. DOI
19. Zhu, X. L.; Bai, Y.; Liu, X. Q.; Chen, X. M. Ferroelectric phase transition and low-temperature dielectric relaxations in $Sr_4(La_{1-x}Sm_x)_2Ti_4Nb_6O_{30}$ ceramics. *J. Appl. Phys.* **2011**, *110*, 114101. DOI
20. Zhu, X. L.; Li, K.; Chen, X. M.; Green, D. J. Ferroelectric transition and low-temperature dielectric relaxations in filled tungsten bronzes. *J. Am. Ceram. Soc.* **2014**, *97*, 329-38. DOI
21. Huang, C. J.; Li, K.; Liu, X. Q.; Zhu, X. L.; Chen, X. M. Effects of A1/A2-sites occupancy upon ferroelectric transition in $(Sr_xBa_{1-x})Nb_2O_6$ Tungsten bronze ceramics. *J. Am. Ceram. Soc.* **2014**, *97*, 507-12. DOI
22. Tidey, J. P.; Dey, U.; Sanchez, A. M.; et al. Structural origins of dielectric anomalies in the filled tetragonal tungsten bronze $Sr_2NaNb_5O_{15}$. *Commun. Mater.* **2024**, *5*, 508. DOI
23. Cao, L.; Wang, Y.; Yuan, Y.; et al. Low temperature relaxor, polarization dynamics and energy storage properties of $Ca_{0.28}Ba_{0.72}Nb_2O_6$ tungsten bronze ceramics. *Chem. Eng. J.* **2024**, *479*, 147664. DOI

24. Peng, H.; Liu, Z.; Fu, Z.; et al. Superior energy density achieved in unfilled tungsten bronze ferroelectrics via multiscale regulation strategy. *Adv. Sci.* **2023**, *10*, e2300227. DOI PubMed PMC
25. Hou, S.; Wang, X.; Liu, X.; et al. Significant increase in comprehensive energy storage performances of $Ca_{0.5}(Sr_{0.5}Ba_{0.5})_2Nb_5O_{15}$-based tungsten bronze relaxor ceramics. *J. Eur. Ceram. Soc.* **2023**, *43*, 6854-63. DOI
26. Xu, S.; Shen, S.; Huang, C.; et al. Enhancing energy storage performance in lead-free bismuth sodium niobate-based tungsten bronze ceramics through relaxor tuning. *ACS. Appl. Mater. Interfaces.* **2023**, *15*, 11642-51. DOI
27. Li, W.; Hao, J.; Li, W.; et al. Electrical properties and luminescence properties of $0.96(K_{0.48}Na_{0.52})(Nb_{0.95}Sb_{0.05})$-$0.04Bi_{0.5}(Na_{0.82}K_{0.18})_{0.5}ZrO_3$-xSm lead-free ceramics. *J. Adv. Ceram.* **2020**, *9*, 72-82. DOI
28. Roukos, R.; Zaiter, N.; Chaumont, D. Relaxor behaviour and phase transition of perovskite ferroelectrics-type complex oxides $(1-x)Na_{0.5}Bi_{0.5}TiO_{3-x}CaTiO_3$ system. *J. Adv. Ceram.* **2018**, *7*, 124-42. DOI
29. Li, X.; Du, Y.; Ge, L.; et al. Engineering polarization in the ferroelectric electrocatalysts to boost water electrolysis. *Adv. Funct. Mater.* **2023**, *33*, 2210194. DOI
30. Li, R.; Pu, Y.; Zhang, Q.; et al. The relationship between enhanced dielectric property and structural distortion in Ca doped $Ba_2NaNb_5O_{15}$ tungsten bronze ceramics. *J. Eur. Ceram. Soc.* **2020**, *40*, 4509-16. DOI
31. Fleury, P. A. The effects of soft modes on the structure and properties of materials. *Annu. Rev. Mater. Sci.* **1976**, *6*, 157-80. DOI
32. Liu, J.; Li, F.; Zeng, Y.; et al. Insights into the dielectric response of ferroelectric relaxors from statistical modeling. *Phys. Rev. B.* **2017**, *96*, 054115. DOI
33. Liu, L.; Ren, S.; Zhang, J.; Peng, B.; Fang, L.; Wang, D. Revisiting the temperature-dependent dielectric permittivity of $Ba(Ti_{1-x}Zr_x)O_3$. *J. Am. Ceram. Soc.* **2018**, *101*, 2408-16. DOI
34. Zhong, X. Y.; Yan, G. W.; Chen, Z. H. Structure and energy storage properties of $(1-x)Ba_{0.98}Li_{0.02}TiO_3$ based ceramics with $xBi(Mg_{1/2}Sn_{1/2})O_3$ addition. *J. Alloys. Compd.* **2022**, *891*, 161855. DOI
35. Cao, L.; Yuan, Y.; Yang, Z.; Li, E.; Zhang, S. Crystal structure, relaxor behaviors and energy storage performance of $(Sr_{0.7}Ba_{0.3})_5LaNb_7Ti_3O_{30}$ tungsten bronze ceramics. *Ceram. Int.* **2020**, *46*, 6108-14. DOI
36. Aamlid, S. S.; Selbach, S. M.; Grande, T. Structural evolution of ferroelectric and ferroelastic barium sodium niobate tungsten bronze. *Inorg. Chem.* **2020**, *59*, 8514-21. DOI PubMed PMC
37. Yao, Y. B.; Mak, C. L.; Ploss, B. Phase transitions and electrical characterizations of $(K_{0.5}Na_{0.5})_{2x}(Sr_{0.6}Ba_{0.4})_{5-x}Nb_{10}O_{30}$ (KNSBN) ceramics with 'unfilled'and 'filled'tetragonal tungsten-bronze (TTB) crystal structure. *J. Eur. Ceram. Soc.* **2012**, *32*, 4353-61. DOI
38. Jiang, X.; Hao, H.; Zhou, J.; et al. Optimized energy storage properties of $BaTiO_3$-based ceramics with enhanced grain boundary effect. *J. Mater. Sci. Mater. Electron.* **2021**, *32*, 14328-36. DOI
39. Zhang, T. F.; Tang, X. G.; Huang, X. X.; Liu, Q. X.; Jiang, Y. P.; Zhou, Q. F. High-temperature dielectric relaxation behaviors of relaxer-like $PbZrO_3$-$SrTiO_3$ ceramics for energy-storage applications. *Energy. Technol.* **2016**, *4*, 633-40. DOI
40. Viehland, D.; Jang, S. J.; Cross, L. E.; Wuttig, M. Freezing of the polarization fluctuations in lead magnesium niobate relaxors. *J. Appl. Phys.* **1990**, *68*, 2916-21. DOI
41. Feng, W. B.; Zhu, X. L.; Liu, X. Q.; et al. Relaxor nature in $Ba_5RZr_3Nb_7O_{30}$ (R = La, Nd, Sm) tetragonal tungsten bronze new system. *J. Am. Ceram. Soc.* **2018**, *101*, 1623-31. DOI
42. Ogihara, H.; Randall, C. A.; Trolier-Mckinstry, S. High-energy density capacitors utilizing $0.7BaTiO_3$-$0.3BiScO_3$ ceramics. *J. Am. Ceram. Soc.* **2009**, *92*, 1719-24. DOI
43. Spasojevic, I.; Sauthier, G.; Caicedo, J. M.; Verdaguer, A.; Domingo, N. Oxidation processes at the surface of $BaTiO_3$ thin films under environmental conditions. *Appl. Surf. Sci.* **2021**, *565*, 150288. DOI
44. Idriss, H. On the wrong assignment of the XPS O1s signal at 531-532 eV attributed to oxygen vacancies in photo- and electro-catalysts for water splitting and other materials applications. *Surf. Sci.* **2021**, *712*, 121894. DOI
45. Qi, H.; Xie, A.; Tian, A.; Zuo, R. Superior energy-storage capacitors with simultaneously giant energy density and efficiency using nanodomain engineered $BiFeO_3$-$BaTiO_3$-$NaNbO_3$ lead-free bulk ferroelectrics. *Adv. Energy. Mater.* **2020**, *10*, 1903338. DOI